

See discussions, stats, and author profiles for this publication at: <https://www.researchgate.net/publication/252914610>

# Accounting for Reynolds stress and dissipation rate anisotropies in inertial and noninertial frames

Article in *Physics of Fluids* · March 1998

DOI: 10.1063/1.869593

CITATIONS

20

READS

145

3 authors, including:



**Gilmar Mompean**

University of Lille Nord de France

117 PUBLICATIONS 963 CITATIONS

[SEE PROFILE](#)



**T. B. Gatski**

207 PUBLICATIONS 8,290 CITATIONS

[SEE PROFILE](#)

Some of the authors of this publication are also working on these related projects:



Temporal Large-Eddy Simulation (TLES) [View project](#)



Transient aspects of the polymer induced drag reduction phenomenon [View project](#)

# Accounting for Reynolds stress and dissipation rate anisotropies in inertial and noninertial frames

T. Jongen and G. Mompean

*Fluid Mechanics Laboratory, Swiss Federal Institute of Technology, 1015 Lausanne, Switzerland*

T. B. Gatski

*NASA Langley Research Center, Hampton, Virginia 23681*

(Received 3 December 1996; accepted 14 November 1997)

This paper presents a general procedure for including added effects, such as turbulent dissipation rate anisotropies, into algebraic stress formulations in both inertial and noninertial frames of reference. Explicit algebraic stress models, which assume an isotropic turbulent dissipation rate, have been developed previously and extended for application to noninertial frames. Independently, anisotropic dissipation rate models have also been developed. Recently, an algebraic, anisotropic dissipation rate model has been developed and used in conjunction with a full Reynolds stress closure. Unfortunately, in the theoretical formulations used previously for explicit algebraic models, the combination of the algebraic stress and algebraic dissipation rate models only appeared possible for inertial frames. The alternative procedure outlined here remedies this problem and allows for the construction of a composite model for both inertial and noninertial frames. This new composite model formulation is tested in homogeneous shear with and without rotation, and in strongly rotating channel and pipe flows using different types of anisotropic dissipation rate models.

© 1998 American Institute of Physics. [S1070-6631(98)01603-1]

## I. INTRODUCTION

Turbulent flows in noninertial reference frames are of considerable interest in a variety of industrial applications. However, the success of a computational analysis of such flow phenomena relies heavily on the choice of turbulence model. It is well-known that, without some modifications, conventional isotropic eddy-viscosity models fail to predict the effect of noninertial forces on turbulence, whereas second-moment closures, for example, are able to account for noninertial effects in a systematic way.

Explicit algebraic stress models (EASMs) have been developed which are nonlinear extensions to an isotropic eddy-viscosity two-equation model. The EASM allows for the inclusion of stress anisotropies and can be developed<sup>1</sup> from a rigorous mathematical basis, while still keeping the associated computational cost comparable to that of two-equation models. Previous results have shown that this approach is a viable approximation to the full Reynolds stress closure for a variety of engineering flows. An extension to this EASM in inertial frames, which accounts for dissipation rate anisotropies in a systematic way has been recently developed,<sup>2</sup> and is based on an analysis of the exact transport equation for the dissipation rate tensor.<sup>3</sup>

In this study, an alternative development of the algebraic stress formulation is presented which explicitly represents the scalar coefficients of the integrity basis as functions of the invariants formed by the products of the turbulent anisotropy field and the mean strain rate and rotation rate fields. This recasting of the integrity basis polynomials used previously<sup>1</sup> allows for the projection of turbulent anisotropy fields, such as the dissipation rate anisotropy, onto the same

basis field as the Reynolds stresses. Composite algebraic stress models (CASMs) can then be developed for noninertial frames whereas previously it appeared necessary to revert to added terms in the polynomial basis representation.

With the introduction of anisotropic dissipation rate models, it is desirable from a practical standpoint to evaluate them in a variety of inertial and noninertial flows. The development presented here now allows for the inclusion of algebraic anisotropic dissipation rate models in noninertial frames. The formalism used is rather general and it is shown that different types of models can be incorporated into the framework outlined.

Finally, in order to initiate the validation of the procedure outlined, homogeneous shear flow with rotation as well as rotating channel and pipe flows will be studied. The spanwise rotating channel flow case used is an extension of previous work in that (1) it uses new DNS data obtained by Lamballais *et al.*<sup>4</sup> for rotation numbers that are higher than those studied previously<sup>5</sup> and (2) the equations are integrated up to the wall, whereas most of the previous computations were limited to wall-function boundary conditions that are not suitable for (strongly) rotating flows where regions of relaminarization can occur. The wide variation of flow behavior across the channel (turbulent to laminar) provides a challenging test of the models and identifies the crucial components of any model that will predict such behavior. The axially rotating pipe flow case studied adds an additional level of complexity since the fully developed axisymmetric mean flow consists of both axial and azimuthal components. Experimental data are available<sup>6</sup> for three different pipe rotation rates. Once again, wall-function boundary conditions

are not used and the equations are integrated directly up to the pipe wall.

## II. COMPOSITE ALGEBRAIC STRESS MODEL

Both anisotropic stress and dissipation rate effects are merged into a composite formulation through explicit algebraic relationships for the stress and dissipation rate tensors. The development of how these extra effects appear in the formulation of the mean flow and turbulent transport equations is presented for noninertial frames of reference.

The mean quantities of an incompressible turbulent flow are obtained from a solution of the Reynolds averaged Navier–Stokes (RANS) equations valid in an arbitrary non-inertial reference frame

$$\frac{\partial \bar{u}_j}{\partial x_j} = 0 \quad (1)$$

and

$$\frac{D\bar{u}_i}{Dt} = -\frac{1}{\rho} \frac{\partial \bar{p}}{\partial x_i} + \nu \frac{\partial^2 \bar{u}_i}{\partial x_j \partial x_j} - \frac{\partial \tau_{ij}}{\partial x_j} - 2\Omega_m e_{ijm} \bar{u}_j, \quad (2)$$

where  $D/Dt = \partial/\partial t + \bar{u}_j \partial/\partial x_j$ ,  $\bar{u}_i$ ,  $\bar{p}$ , and  $\rho$  are the mean velocity, mean pressure (which includes the centrifugal force term), and density, respectively,  $\nu$  is the kinematic viscosity, and  $\Omega_m$  is the rotation rate vector of the reference frame. The right-hand side of the equation also contains the correlation tensor  $\tau_{ij} \equiv \overline{u'_i u'_j}$ , which requires closure. For the higher-order closures, the transport equation for the  $\tau_{ij}$  correlation is used,

$$\frac{D\tau_{ij}}{Dt} = P_{ij} + \Pi_{ij} - \varepsilon_{ij} - 2\Omega_m (e_{mkj} \tau_{ik} + e_{mki} \tau_{jk}) + \mathcal{D}_{ij}. \quad (3)$$

In addition to the Coriolis effects, the right-hand side represents the rate of change of  $\tau_{ij}$  produced by the turbulent production  $P_{ij}$ , the pressure strain-rate correlation  $\Pi_{ij}$ , the turbulent dissipation rate  $\varepsilon_{ij}$ , and the turbulent and viscous diffusion  $\mathcal{D}_{ij}$ .

The deviatoric part of the dissipation rate is generally absorbed into the pressure-strain correlation to account for any anisotropic dissipation rate effects. However, as will be discussed shortly, when models for the anisotropic dissipation rate  $\varepsilon_{ij}$  are utilized, this assimilation into the pressure-strain correlation is no longer necessary.

The trace of Eq. (3) results in the turbulent kinetic energy equation given by

$$\frac{DK}{Dt} = \mathcal{P} - \varepsilon + \mathcal{D}_K, \quad (4)$$

where the right-hand side represents the transport of  $K$  by the turbulent production  $\mathcal{P} \equiv P_{ii}/2 = -\tau_{ij} \partial \bar{u}_i / \partial x_j$ , the isotropic turbulent dissipation rate,  $\varepsilon \equiv \varepsilon_{ii}/2$ , and the turbulent and viscous diffusion  $\mathcal{D}_K \equiv \mathcal{D}_{ii}/2$ . Consistent with the simplification that results from the two-equation formulation, a simple model for  $\mathcal{D}_K$  is usually used:

$$\mathcal{D}_K = \frac{\partial}{\partial x_j} \left[ \left( \nu + \frac{\nu_t}{\sigma_K} \right) \frac{\partial K}{\partial x_j} \right], \quad (5)$$

with

$$\nu_t = C_\mu \frac{K^2}{\varepsilon} \quad (6)$$

and  $\sigma_K = 1$  and  $C_\mu$  is in the range 0.08–0.09. The turbulent dissipation rate is obtained from a solution of a modeled transport equation which will be presented in the next section.

The derivations of the EASM,<sup>1</sup> which assumed an isotropic dissipation rate, and of the algebraic dissipation rate model<sup>3</sup> (ADRM) have been presented previously. These derivations both used an integrity basis tensorial representation to replace the implicit relation for both the Reynolds stress anisotropy and the turbulent dissipation rate anisotropy derived from their respective transport equations. While this procedure is perfectly valid, it masks the generality that can be associated with such explicit representations. In the following, a more general development will be presented.

We consider models for the deviatoric part of the pressure-strain rate correlation tensor  $\Pi_{ij}$  that are tensorially linear in the anisotropy tensor  $b_{ij}$ ,

$$\begin{aligned} \Pi_{ij} = & -C_1 \varepsilon b_{ij} + C_2 K S_{ij} + C_3 K (b_{ik} S_{jk} + b_{jk} S_{ik} \\ & - \frac{2}{3} b_{mn} S_{mn} \delta_{ij}) - C_4 K (b_{ik} W_{kj} - W_{ik} b_{kj}), \end{aligned} \quad (7)$$

where

$$b_{ij} = \frac{(\tau_{ij} - \frac{2}{3} K \delta_{ij})}{2K}, \quad (8)$$

$$S_{ij} = \frac{1}{2} \left( \frac{\partial \bar{u}_i}{\partial x_j} + \frac{\partial \bar{u}_j}{\partial x_i} \right), \quad \omega_{ij} = \frac{1}{2} \left( \frac{\partial \bar{u}_i}{\partial x_j} - \frac{\partial \bar{u}_j}{\partial x_i} \right), \quad (9)$$

$$W_{ij} = \omega_{ij} + \epsilon_{mji} \Omega_m. \quad (10)$$

The absolute vorticity tensor  $W_{ij}$  is the vorticity tensor  $\omega_{ij}$  relative to an inertial frame. With this model for  $\Pi_{ij}$ , the Reynolds stress equation (3) can be written as

$$\begin{aligned} & \left( \frac{D\tau_{ij}}{Dt} - \frac{\tau_{ij}}{K} \frac{DK}{Dt} \right) - \left( \mathcal{D}_{ij} - \frac{\tau_{ij}}{K} \mathcal{D}_K \right) \\ & = -2K \left[ \frac{b_{ij}}{\alpha_4 \tau} + \alpha_3 \left( b_{ik} S_{kj} + S_{ik} b_{kj} - \frac{2}{3} b_{mn} S_{mn} \delta_{ij} \right) \right. \\ & \quad \left. - \alpha_2 (b_{ik} \bar{W}_{kj} - \bar{W}_{ik} b_{kj}) + \alpha_1 S_{ij} + \frac{d_{ij}}{\tau} \right], \end{aligned} \quad (11)$$

where the equation for the turbulent kinetic energy (4) has been used,

$$d_{ij} = \frac{(\varepsilon_{ij} - \frac{2}{3} \varepsilon \delta_{ij})}{2\varepsilon}, \quad (12)$$

$$\alpha_1 = \frac{1}{2} \left( \frac{4}{3} - C_2 \right), \quad \alpha_2 = \frac{1}{2} (2 - C_4), \quad \alpha_3 = \frac{1}{2} (2 - C_3), \quad (13)$$

$$g = \left( \frac{C_1}{2} + \frac{\mathcal{P}}{\varepsilon} - 1 \right)^{-1}$$

and

$$\bar{W}_{ij} = \omega_{ij} + \bar{c}_\omega \epsilon_{mji} \Omega_m, \quad \bar{c}_\omega = \frac{C_4 - 4}{C_4 - 2} \quad (14)$$

with  $\tau = K/\epsilon$  a turbulent time scale, and  $\alpha_4 = g$ . Depending on how the anisotropic dissipation rate model under consideration is formulated, the form of  $\alpha_4$  may change (see Eq. (35)). The other coefficients  $\alpha_i$  are all determined by the choice of pressure-strain rate model given in (7). For the purposes of this study, the Speziale, Sarkar and Gatski (SSG) model<sup>7</sup> is chosen here with coefficients

$$C_1 = 3.4 + 1.8 \frac{\mathcal{P}}{\epsilon}, \quad C_2 = 0.36, \quad C_3 = 1.25, \quad C_4 = 0.40. \quad (15)$$

The starting point for the development of an algebraic stress model (ASM) is to assume that the stress anisotropy  $b_{ij}$  has reached an equilibrium state given by

$$\frac{Db_{ij}}{Dt} = \frac{1}{2K} \left( \frac{D\tau_{ij}}{Dt} - \frac{\tau_{ij}}{K} \frac{DK}{Dt} \right) = 0 \quad (16)$$

and to assume that the Reynolds stress turbulent transport and diffusion  $\mathcal{D}_{ij}$ , and the turbulent kinetic energy transport and diffusion  $\mathcal{D}_K$ , are related by  $\mathcal{D}_{ij} = (\tau_{ij}/K)\mathcal{D}_K$ . Equation (11) then reduces to

$$\begin{aligned} \frac{b_{ij}}{\alpha_4 \tau} + \alpha_3 \left( b_{ik} S_{kj} + S_{ik} b_{kj} - \frac{2}{3} b_{mn} S_{mn} \delta_{ij} \right) \\ - \alpha_2 (b_{ik} \bar{W}_{kj} - \bar{W}_{ik} b_{kj}) = -\alpha_1 S_{ij} - \frac{d_{ij}}{\tau}. \end{aligned} \quad (17)$$

For ASMs that are consistently derived from full Reynolds stress closures in two-dimensional flows, the next step in obtaining an *explicit* representation for the *implicit* expression shown in (17) is to expand in a tensorial basis<sup>1</sup> which consists of terms that are either linear or quadratic in the mean strain rate  $S_{ij}$  and rotation rate tensors  $\bar{W}_{ij}$ . The general form of this polynomial representation is given by

$$b_{ij} = \sum_{\lambda} G^{(\lambda)} T_{ij}^{(\lambda)}, \quad (18)$$

where

$$\begin{aligned} T_{ij}^{(1)} &= S_{ij}, \quad T_{ij}^{(2)} = (S_{ik} \bar{W}_{kj} - \bar{W}_{ik} S_{kj}), \\ T_{ij}^{(3)} &= (S_{ik} S_{kj} - \frac{1}{3} S_{mn} S_{mn} \delta_{ij}) \end{aligned} \quad (19)$$

form the three-term integrity basis ( $\lambda = 1, 2, 3$ ) for functions of a symmetric and an antisymmetric tensor, and  $G^{(\lambda)}$  are, in general, scalar functions of the irreducible invariants of  $b_{ij}$ ,  $S_{ij}$ ,  $\bar{W}_{ij}$ , and also  $d_{ij}$  as (17) suggests. Note that this three-term expansion is only formally valid for two-dimensional flows. For three-dimensional flows, a 10-term basis would be required; however, Gatski and Speziale<sup>1</sup> have shown that the three-term basis is a truncation of the full tensorial expansion of the lowest order. For this reason and because the full 10-term basis is too cumbersome for practical calculations, the three-term basis has been recommended for both two- and three-dimensional flows.

When the dissipation rate anisotropy is not neglected it can also be represented in terms of the three-term basis  $\mathbf{T}^{(\lambda)}$ . In general, this integrity basis representation is given by<sup>8</sup>

$$d_{ij} = \sum_{\lambda} L^{(\lambda)} T_{ij}^{(\lambda)}, \quad (20)$$

where the scalar functions are

$$\begin{aligned} L^{(1)} &= \frac{\{\mathbf{dS}\}}{\{\mathbf{S}^2\}}, \\ L^{(2)} &= \frac{\{\mathbf{dWS}\}}{\{\mathbf{S}^2\}\{\bar{\mathbf{W}}^2\}}, \\ L^{(3)} &= \frac{6\{\mathbf{dS}^2\}}{\{\mathbf{S}^2\}^2}. \end{aligned} \quad (21)$$

This expansion for  $d_{ij}$  can be inserted into (17) and similar basis terms combined. The resulting general expression for the three scalar functions  $G^{(\lambda)}$  are

$$\begin{aligned} G^{(1)} &= -\alpha_4 \tau C_\mu^* \left( \alpha_1 + \frac{\{\mathbf{dS}\}}{\tau\{\mathbf{S}^2\}} + 2\alpha_4 \alpha_2 \frac{\{\mathbf{dWS}\}}{\{\mathbf{S}^2\}} \right. \\ &\quad \left. - 2\alpha_4 \alpha_3 \frac{\{\mathbf{dS}^2\}}{\{\mathbf{S}^2\}} \right), \\ G^{(2)} &= \alpha_4 \tau \left( \alpha_2 G^{(1)} - \frac{\{\mathbf{dWS}\}}{\tau\{\mathbf{S}^2\}\{\bar{\mathbf{W}}^2\}} \right), \\ G^{(3)} &= -\alpha_4 \tau \left( 2\alpha_3 G^{(1)} + \frac{6\{\mathbf{dS}^2\}}{\tau\{\mathbf{S}^2\}^2} \right), \end{aligned} \quad (22)$$

where

$$C_\mu^* = [1 - 2(\alpha_4 \tau)^2 \alpha_2^2 \{\bar{\mathbf{W}}^2\} - \frac{2}{3}(\alpha_4 \tau)^2 \alpha_3^2 \{\mathbf{S}^2\}]^{-1}. \quad (23)$$

The final polynomial expression for  $b_{ij}$ , which includes the effects of anisotropic dissipation rate, is then given by

$$\begin{aligned} b_{ij} &= G^{(1)} S_{ij} + G^{(2)} (S_{ik} \bar{W}_{kj} - \bar{W}_{ik} S_{kj}) \\ &\quad + G^{(3)} (S_{ik} S_{kj} - \frac{1}{3} S_{kl} S_{kl} \delta_{ij}). \end{aligned} \quad (24)$$

All that remains is the evaluation of the invariants  $\{\mathbf{dS}\}$ ,  $\{\mathbf{dS}^2\}$ , and  $\{\mathbf{dWS}\}$ .

### III. DISSIPATION RATE MODELS

The formalism presented in the last section was intended to highlight the underlying assumptions associated with the composite model rather than to isolate on a particular dissipation rate model. However, it is now necessary to focus on the models to be tested and how they are accommodated into the framework presented in the last section.

Two anisotropic dissipation rate models will be tested in the composite algebraic stress framework. One is the model of Speziale and Gatski<sup>3</sup> and the other is the model of Hallbäck *et al.*<sup>9</sup>

The Speziale and Gatski<sup>3</sup> model can be easily introduced into the composite algebraic stress framework just presented. Their explicit algebraic dissipation rate model (ADRM) in the noninertial case is given by

$$d_{ij} = -\frac{2g_\varepsilon\tau}{15}C_{\mu\varepsilon}^*\left[S_{ij} + \beta_1\tau(S_{ik}W_{kj}^* - W_{ik}^*S_{kj}) + 2\beta_2\tau\left(S_{ik}S_{kj} - \frac{1}{3}S_{mn}S_{mn}\delta_{ij}\right)\right], \quad (25)$$

where

$$C_{\mu\varepsilon}^* = [1 - 2(g_\varepsilon\tau)^2\beta_1^2\{\mathbf{W}^{*2}\} - \frac{2}{3}(g_\varepsilon\tau)^2\beta_2^2\{\mathbf{S}^2\}]^{-1}, \quad (26)$$

$$W_{ij}^* = \omega_{ij} + c_\omega^*\epsilon_{mji}\Omega_m, \quad (27)$$

with

$$\beta_1 = \frac{26}{55}g_\varepsilon, \quad \beta_2 = \frac{8}{11}g_\varepsilon, \quad g_\varepsilon = \left(C_{\varepsilon 5} + \frac{\mathcal{P}}{\varepsilon} - 1\right)^{-1}, \quad (28)$$

$$C_{\varepsilon 5} = 5.8, \quad c_\omega^* = \frac{81}{26}.$$

With the explicit relation (25), it is possible to form the invariant relations  $\{\mathbf{dS}\}$ ,  $\{\mathbf{dS}^2\}$ , and  $\{\mathbf{d}\bar{\mathbf{W}}\mathbf{S}\}$  that are needed in (22),

$$\begin{aligned} \{\mathbf{dS}\} &= -\frac{2}{15}C_{\mu\varepsilon}^*g_\varepsilon\tau\{\mathbf{S}^2\}, \\ \{\mathbf{dS}^2\} &= -\frac{2}{45}C_{\mu\varepsilon}^*g_\varepsilon\tau^2\beta_2\{\mathbf{S}^2\}^2, \\ \{\mathbf{d}\bar{\mathbf{W}}\mathbf{S}\} &= -\frac{2}{15}C_{\mu\varepsilon}^*g_\varepsilon\tau^2\beta_1\{\mathbf{W}^*\bar{\mathbf{W}}\}\{\mathbf{S}^2\}. \end{aligned} \quad (29)$$

The  $G^{(\lambda)}$  for the noninertial composite algebraic stress model are then

$$\begin{aligned} G^{(1)} &= -\alpha_1\alpha_4\tau C_{\mu}^*\{1 + \mathcal{A}[1 + 2\alpha_2\alpha_4\tau^2\beta_1\{\mathbf{W}^*\bar{\mathbf{W}}\} \\ &\quad - \frac{2}{3}\alpha_3\alpha_4\tau^2\beta_2\{\mathbf{S}^2\}]\}, \\ G^{(2)} &= \alpha_4\tau\left[\alpha_2G^{(1)} - \mathcal{A}\tau\alpha_1\beta_1\frac{\{\mathbf{W}^*\bar{\mathbf{W}}\}}{\{\bar{\mathbf{W}}^2\}}\right], \\ G^{(3)} &= -2\alpha_4\tau[\alpha_3G^{(1)} + \mathcal{A}\tau\alpha_1\beta_2], \end{aligned} \quad (30)$$

where

$$\mathcal{A} = -\frac{2g_\varepsilon}{15\alpha_1}C_{\mu\varepsilon}^*. \quad (31)$$

This explicit algebraic relationship is now coupled with an equation for the turbulent kinetic energy (4) and for the turbulent dissipation rate to be presented shortly. In the inertial case where  $\mathbf{W}^* = \bar{\mathbf{W}}$ , the results given in (30) reduce to that given by Xu and Speziale<sup>2</sup> obtained previously in a different manner. In the noninertial case, it is evident that the ADRM expression (25) for  $d_{ij}$  is not of the form (20) anymore, since the tensor bases are now different. It would therefore seem necessary to introduce one more independent tensor into the expression of  $b_{ij}$ , and derive the corresponding integrity base for one symmetric tensor  $\mathbf{S}$  and two anti-symmetric ten-

sors  $\mathbf{W}^*$  and  $\bar{\mathbf{W}}$ . In addition to introducing another degree of complexity, it would contradict the original assumption of  $\mathbf{b} = \mathbf{b}(\mathbf{S}, \bar{\mathbf{W}})$ .

One of the major points of the present study is to show how noninertial effects can be consistently introduced. Since the stress anisotropy tensor is expressed in the tensor basis  $\mathbf{T}^{(\lambda)}$ , it is necessary to express every other tensor in the same basis. This is easily done by “projecting” expression (25) for  $d_{ij}$  onto the same tensor base as  $b_{ij}$  through relations (20) and (21), which are a mathematical identity giving the expansion of any tensor into the tensor base  $\mathbf{T}^{(\lambda)}$ . As will now be shown, this general principle can be applied to any other tensor expression for the dissipation rate.

Another algebraic dissipation rate model is due to Hallbäck *et al.*<sup>9</sup> This model can be written as

$$d_{ij} = fb_{ij} + d'_{ij}, \quad (32)$$

where

$$f = \frac{1}{2} - 3II_b, \quad (33)$$

$$d'_{ij} = -\frac{3}{2}(b_{ik}b_{kj} + \frac{2}{3}II_b\delta_{ij}), \quad (34)$$

and  $II_b = -b_{mn}b_{mn}/2$  is the second invariant of the stress anisotropy. The term proportional to the stress anisotropy  $b_{ij}$  can be easily combined with the corresponding  $b_{ij}$  term on the left side of (17). This simply changes the definition of  $\alpha_4$  from  $g$  given in (13) to

$$\alpha_4 = \frac{g}{1 + gf}. \quad (35)$$

Since  $f \geq 1/2$  and  $g > 0$ , the coefficient  $\alpha_4$  is always positive for this model. When the dependence of  $d'_{ij}$  on  $b_{ij}$  is retained implicitly, the quadratic term can be easily projected on the tensor basis as defined in (20) and (21), where  $d_{ij}$  is replaced by  $d'_{ij}$  and the corresponding invariants  $\{\mathbf{d}'\mathbf{S}\}$ ,  $\{\mathbf{d}'\mathbf{S}^2\}$ , and  $\{\mathbf{d}'\bar{\mathbf{W}}\mathbf{S}\}$  formed.

Similar arguments can be used for other anisotropic dissipation rate models. For example, the model of Hanjalić and Launder<sup>10</sup> which has  $d_{ij}$  proportional to the stress anisotropy  $b_{ij}$  is easily included in this CASM formulation. However, their model is dependent on the turbulent Reynolds number and for the flows examined in the next section, the effect on the anisotropic dissipation rate is minimal, and will not be considered for the test cases presented here.

The anisotropic dissipation rate models that have been discussed need to be coupled with a transport equation for the isotropic dissipation rate  $\varepsilon$ . The form of this equation which is applicable to the models is given by

$$\frac{D\varepsilon}{Dt} = C_{\varepsilon 1}^*\frac{\varepsilon}{K}\mathcal{P} - f_\varepsilon C_{\varepsilon 2}\frac{\varepsilon^2}{K} + \frac{\partial}{\partial x_k}\left[\left(\nu + \frac{\nu_t}{\sigma_\varepsilon}\right)\frac{\partial \varepsilon}{\partial x_k}\right], \quad (36)$$

where

$$C_{\varepsilon 1}^* = C_{\varepsilon 1} + \beta_\varepsilon\frac{\{\mathbf{dS}\}}{\{\mathbf{bS}\}}, \quad (37)$$

$$f_\varepsilon = \left[1 - \exp\left(-\frac{y^+}{A^+}\right)\right]^2, \quad y^+ = \frac{y u_\tau}{\nu}, \quad (38)$$

with  $C_{\varepsilon 2} = 1.83$ ,  $u_\tau$  is the shear velocity, and  $y$  is taken as the distance normal to the surface. For the ADRM the remaining coefficients are given by

$$C_{\varepsilon 1} = 1.0, \quad \beta_\varepsilon = 1.21, \quad \sigma_\varepsilon = 1.30, \quad A^+ = 6.5, \quad C_\mu = 0.094, \quad (39)$$

and for the Hallbäck model these coefficients are

$$C_{\varepsilon 1} = 1.44, \quad \beta_\varepsilon = 0, \quad \sigma_\varepsilon = 1.51, \quad A^+ = 5.5, \quad C_\mu = 0.081. \quad (40)$$

These coefficient values are obtained from a calibration of the models with fully developed channel flow data.

When an anisotropic turbulent dissipation rate formulation is used, the isotropic dissipation rate equation can retain dissipation rate anisotropies; thus, the form of the  $\varepsilon$  equation can be modified. The ADRM of Speziale and Gatski,<sup>3</sup> which is derived from a transport equation for the tensor dissipation rate, reflects this effect through a variable production of dissipation rate coefficient. The invariants required for the determination of  $C_{\varepsilon 1}^*$ ,  $\{\mathbf{bS}\}$  and  $\{\mathbf{dS}\}$ , are obtained from Equations (24) and (29), respectively. In contrast, the Hallbäck model<sup>9</sup> is not derived in this fashion and needs to be coupled with the standard isotropic dissipation rate equation ( $\beta_\varepsilon = 0$ ).

#### IV. RESULTS

The test cases to be studied in order to assess the performance of the dissipation rate models presented in the last section when incorporated into a composite algebraic stress framework are homogeneous shear with rotation, and rotating channel and pipe flows. These test cases are used for validation because they are sufficiently complex to test the fundamental assumptions of the modeling framework without (or with minimal) complications from diffusive effects or questions of numerical methodology.

In homogeneous shear with rotation and rotating channel flow, the mean strain rate and rotation rate tensors reduce to

$$S_{ij} = \frac{1}{2} \begin{pmatrix} 0 & S & 0 \\ S & 0 & 0 \\ 0 & 0 & 0 \end{pmatrix}, \quad \omega_{ij} = \frac{1}{2} \begin{pmatrix} 0 & S & 0 \\ -S & 0 & 0 \\ 0 & 0 & 0 \end{pmatrix}, \quad (41)$$

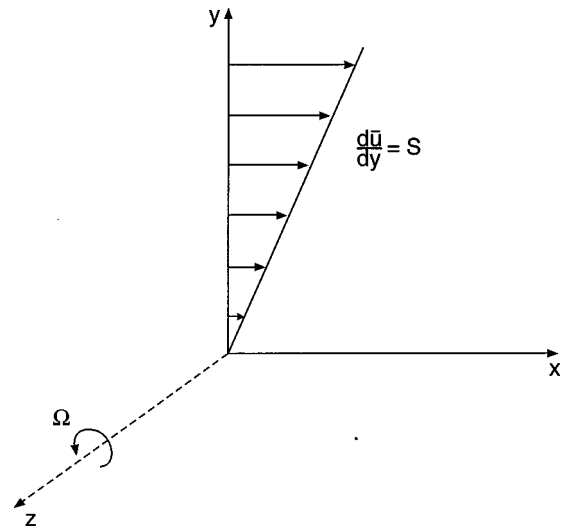


FIG. 1. Schematic of homogeneous shear flow in a rotating frame.

which makes the transport equations and algebraic stress relations amenable to analysis. A schematic of the homogeneous shear flow in the rotating frame is shown in Figure 1. The time evolution of the scaled turbulent kinetic energy using both the Hallbäck<sup>9</sup> model (CASM-HGJ) and the Speziale and Gatski<sup>3</sup> model (CASM-SG) is shown in Figure 2, and compared to the large eddy simulation (LES) data of Bardina, Ferziger and Reynolds.<sup>11</sup> The figure shows that both dissipation rate models are able to accurately predict the non-rotating case as well as the high rotation rate case. For the most energetic case,  $\Omega/S = 0.25$ , both models are unable to accurately predict the initial temporal evolution although both show rapid energetic growth in the time span shown. This early time inaccuracy is due to the “rapid” response of the turbulent shear stress to the mean shear. In the LES simulation, the initial turbulence field was isotropic with no shear. In the early times, the shear stress developed through the redistribution action of the pressure-strain rate correlation. With an algebraic stress formulation, the shear stress is directly related to the mean shear and responds instantaneously to it. Although outside the scope of the present study, this

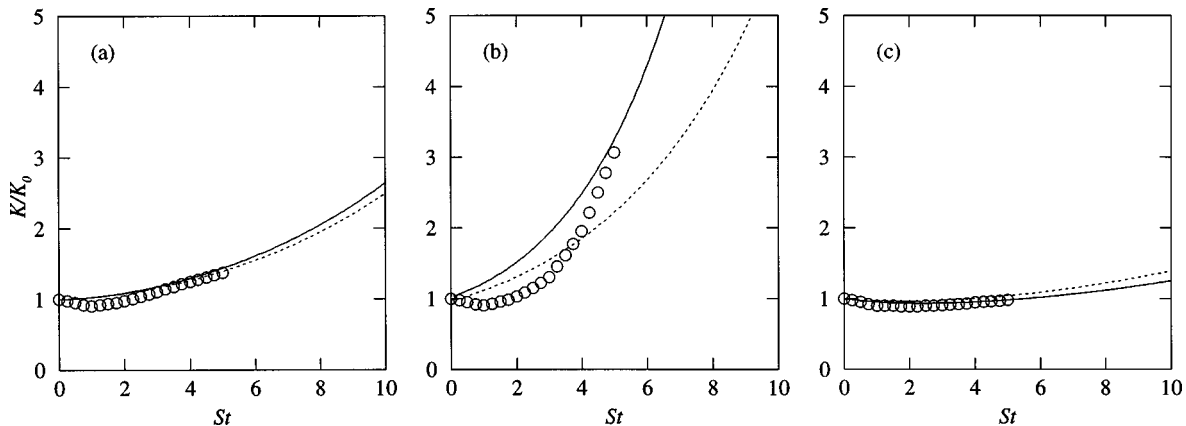


FIG. 2. Time evolution of the turbulent kinetic energy for homogeneous shear flow in a rotating frame for (a)  $\Omega/S = 0$ , (b)  $\Omega/S = 0.25$  and (c)  $\Omega/S = 0.5$ .  $\circ$  LES (Ref. 11); —, CASM-SG; ---, CASM-HGJ.

TABLE I. Equilibrium results for homogeneous turbulent shear flow in a rotating frame: Comparison of the predictions of the Hallbäck *et al.*—Ref. 9 (CASM-HGJ) and Speziale and Gatski—Ref. 3 (CASM-SG) models with the large-eddy simulations (Ref. 11) and the physical experiments (Ref. 13).

	Equilibrium values	CASM-HGJ	CASM-SG	Experiments	Large-eddy Simulations
$\Omega/S=0.0$	$b_{11}$	0.184	0.200	0.201	0.30
	$b_{22}$	-0.127	-0.139	-0.147	-0.26
	$b_{12}$	-0.157	-0.153	-0.150	-0.15
$\Omega/S=0.25$	$b_{11}$	0.009	0.009	...	0.06
	$b_{22}$	0.048	0.052	...	0.05
	$b_{12}$	-0.220	-0.237	...	-0.35
$\Omega/S=0.5$	$b_{11}$	-0.166	-0.177	...	-0.27
	$b_{22}$	0.223	0.238	...	0.25
	$b_{12}$	-0.106	-0.096	...	-0.10

problem can be rectified by including nonequilibrium effects into the modeling process such as that suggested by Speziale and Xu.<sup>12</sup> The anisotropy values reached by both the CASM-HGJ and CASM-SG models at equilibrium are shown in Table I and compared with the LES as well as physical experiments.<sup>13</sup> Since the LES results were not defiltered, they tend to overpredict the anisotropy tensor as evidenced by the experimental values in the nonrotating case. Nevertheless, both models do a reasonable job of predicting the equilibrium values for the three rotation rates studied. The CASM-SG model performs better, but this should be expected since both the algebraic stress and dissipation rate models individually were calibrated using these flows.

For the fully developed unidirectional, rotating channel flow case shown in Figure 3, the velocity field is given by  $\bar{u}_i = (U(y), 0, 0)$  and the effective streamwise gradient of the pressure (which includes the centrifugal force term) is constant. The flow is parametrized by the bulk Reynolds number  $Re_b = hU_b/\nu$ , with  $U_b$  as the bulk velocity, and the rotation number  $Ro = 2|\Omega|h/U_b$  with  $\Omega$  the rotation rate of the reference frame ( $\Omega_m = (0, 0, \Omega)$ ). The turbulence models presented in the previous sections are coupled with the transport equations for the turbulent kinetic energy and the turbulent dissipation rate as well as the streamwise momentum equation, and are integrated to steady state by a one-dimensional second-order finite-difference scheme. This simple one-dimensional spatial problem allows for solutions with arbi-

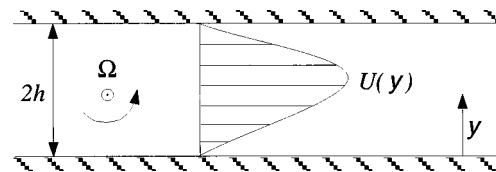


FIG. 3. Schematic of fully developed turbulent channel flow in a rotating frame.

trarily high numerical accuracy by using a sufficient number of points. Here, 200 points were typically used, with highly stretched meshes near the solid walls.

Because the different rotation regimes considered in the DNS study of Lamballais *et al.*<sup>4</sup> were obtained at the same bulk Reynolds number, the pressure gradient in the numerical code was adjusted in order to have  $Re_b = 2500$  at convergence. In the following, results for three different rotation numbers,  $Ro = 0$ ,  $Ro = 0.5$ , and  $Ro = 1.5$  are shown. In the earlier DNS study of Kristoffersen and Andersson,<sup>5</sup> the maximum rotation number studied was 0.5. Thus the DNS data used here significantly increase the validation range for the turbulence closure models. As noted in the last section, the CASMs were integrated to the wall and the calibration was based on fully developed turbulent channel flow<sup>14</sup> at a bulk Reynolds number of 61600.

In addition to the composite models, CASM-HGJ and CASM-SG, tested for the homogeneous shear case, a Coriolis-modified eddy viscosity model<sup>15</sup> (EVM) is also tested. This model is included because it has been evaluated in rotating channel flows<sup>16</sup> but at lower rotation numbers. The EVM differs from the CASMs in that the noninertial modifications are phenomenological rather than theoretically based, and there are no dissipation rate anisotropies included. This will provide an interesting contrast to the theoretical development presented in the previous sections. The Coriolis-modified EVM<sup>15</sup> is based on the Launder–Sharma model<sup>17</sup> with the following Coriolis modification added to the dissipation rate equation:

$$0.4C_{\varepsilon 2}S^2K\left(\frac{\Omega}{S}\right)\left(1 - 2\frac{\Omega}{S}\right), \quad (42)$$

where  $C_{\varepsilon 2} = 1.92$ .

As is well known a standard two equation formulation is not altered in noninertial frames and as such cannot account for system rotation and would not perform well in this case.

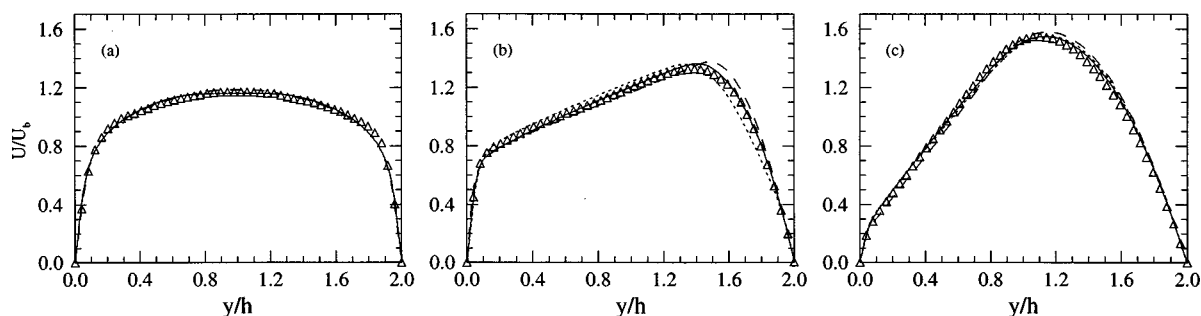


FIG. 4. Mean velocity profiles for (a)  $Ro = 0$ , (b)  $Ro = 0.5$ , and (c)  $Ro = 1.5$ .  $\triangle$  DNS (Ref. 4); —, CASM-SG; ---, CASM-HGJ; -.-, Coriolis-modified EVM.

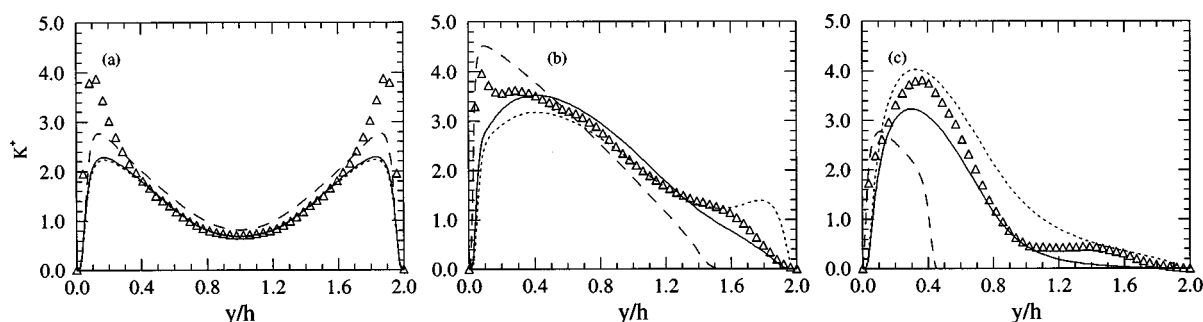


FIG. 5. Turbulent kinetic energy profiles for (a)  $Ro=0$ , (b)  $Ro=0.5$ , and (c)  $Ro=1.5$ .  $\Delta$  DNS (Ref. 4); —, CASM-SG; ---, CASM-HGJ; — · —, Coriolis-modified EVM.

On the other hand, tests with an EASM model on this flow, using an isotropic dissipation rate model, gives similar results as the CASM. As will be shown in the remainder of this section, the essential features of the algebraic stress models, for the accurate prediction of the rotating channel flow, are inherited from the Reynolds stress transport equations. Modifications to the dissipation rate transport equation, either phenomenologically or mathematically based, are not the leading order effect.

The profiles of the mean velocity and turbulent kinetic energy are shown in Figures 4 and 5, respectively. The turbulent kinetic energy, as well as the turbulent stresses to be presented, are scaled by an average friction velocity  $u_\tau$ , which is the half-sum of the friction velocities on both walls. The DNS results show the characteristic linear region of slope  $2\Omega$  in the mean velocity, which leads to a mean absolute vorticity  $(S - 2\Omega)$  that is close to zero. These results also show that the turbulent kinetic energy is higher on the anticyclonic or pressure side ( $y=0$ ) than on the cyclonic or suction side ( $y=2$ ), where relaminarization occurs. In Figure 4, all the models do a good job of predicting the mean velocity fields. At the higher rotation rates, the difference between models is the greatest with the CASM-SG more closely approximating the data. Nevertheless, at  $Ro=1.5$  all the models yield a linear portion of the profile, and a relaminarization on the cyclonic side, characterized by a parabolic velocity profile. For the turbulent kinetic energy shown in Figure 5, the asymmetry of the profile and the higher turbulence intensity on the anticyclonic side of the channel are clearly visible and are consistent with the DNS results. In the case for which  $Ro=0$ , the peaks in turbulent kinetic energy

near the wall are not well predicted for all the models. In the case of the CASMs this is due to the fact that no  $f_\mu$  damping function has been introduced into the eddy viscosity  $\nu_t$  (see Eq. (6)). At  $Ro=0.5$ , the composite models give a better representation of the data than the Coriolis-modified EVM with the CASM-SG model giving the more accurate prediction. For the  $Ro=1.5$  case, the same behavior holds with the EVM effectively damping out the turbulent kinetic energy in the relaminarizing portion of the flow. Both composite models seem to provide the same level of accuracy across the channel.

With the success of the CASM, further investigation of the flow dynamics is worthwhile by examining the total shear stress. The streamwise momentum equation can be integrated with respect to  $y$  and expressed in wall units as

$$-\tau_{12}^+ + \frac{1}{Re_\tau} S^+ = u_{\tau 0}^2 \left[ 1 - \frac{y}{2} \left( 1 + \frac{u_{\tau 2}^2}{u_{\tau 0}^2} \right) \right], \quad (43)$$

where  $u_{\tau 0} = u_\tau|_{y=0}$ ,  $u_{\tau 2} = u_\tau|_{y=2}$ , and  $Re_\tau = hu_\tau/\nu$ . As (43) shows, the total shear must vary linearly across the channel for all rotation rates. The partition of the total shear stress between the turbulent  $\tau_{12}^+$  and viscous  $S^+/Re_\tau$  stresses is illustrated in Figure 6 using CASM-SG. The region of neutral stability, where the velocity profile is linear, is characterized by a turbulent shear stress that varies linearly, and a viscous shear stress that remains constant.

In addition to the turbulent shear stress, the normal Reynolds stresses are significantly affected by the rotation. For the CASM-SG, Figure 7 shows the attenuation of the normal stress components on the relaminarized side of the channel at both nonzero rotation numbers. On the turbulent side, the

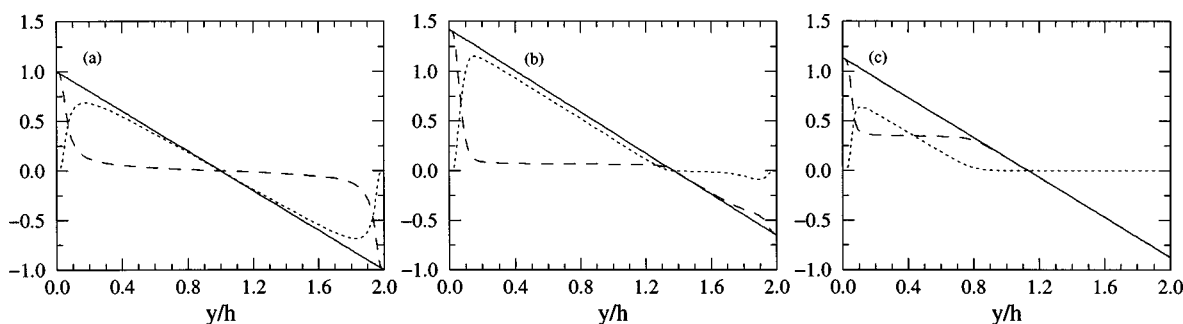


FIG. 6. Partition of the total shear between turbulent and viscous shear stresses: computations by CASM-SG for (a)  $Ro=0$ , (b)  $Ro=0.5$ , and (c)  $Ro=1.5$ . —,  $-\tau_{12}^+ + S^+/Re_\tau$ ; ---,  $-\tau_{12}^+$ ; — · —,  $S^+/Re_\tau$ .



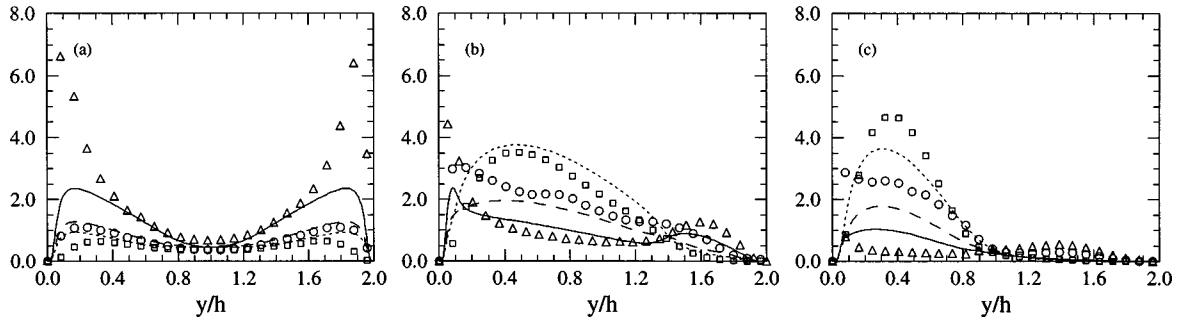


FIG. 7. Turbulent normal stress profiles for (a)  $Ro=0$ , (b)  $Ro=0.5$ , and (c)  $Ro=1.5$ . DNS (Ref. 4) data:  $\Delta$ ,  $\tau_{11}$ ;  $\square$ ,  $\tau_{22}$ ;  $\circ$ ,  $\tau_{33}$ . CASM-SG: —,  $\tau_{11}$ ; ---,  $\tau_{22}$ ; - - -,  $\tau_{33}$ .

streamwise component  $\tau_{11}$  is attenuated relative to the  $Ro=0$  case, and both the  $\tau_{22}$  and  $\tau_{33}$  components are enhanced relative to the  $Ro=0$  case. The most significant effect is on the  $\tau_{22}$  component, but even at the high rotation case the  $\tau_{33}$  component also exceeds the  $\tau_{11}$  component on the anticyclonic side. This result is consistent with the DNS results.

Both the presence of the linear velocity profile and the relaminarization process can be explained. The composite models are derivable from the Reynolds stress model given in (11), and the equilibrium hypothesis that underlies the algebraic stress models is exactly satisfied here ( $\dot{\tau}_{ij} = \dot{K} = 0$ ). The only approximation that is made is  $\mathcal{D}_{ij} = (\tau_{ij}/K)\mathcal{D}_K$ . Recall that the production-to-dissipation rate ratio is defined as

$$\frac{\mathcal{P}}{\varepsilon} \equiv -2\{\mathbf{bS}\}\tau, \quad (44)$$

where the scalar production function  $\{\mathbf{bS}\}$  can be obtained from (11). This yields the following production-to-dissipation rate expression:

$$\frac{\mathcal{P}}{\varepsilon} = 2\bar{\alpha}_1\alpha_4C_\mu^*\{\mathbf{S}^2\}\tau^2 \quad (45)$$

with

$$\begin{aligned} \bar{\alpha}_1 = \alpha_1 + \frac{1}{\{\mathbf{S}^2\}\tau^2} (\{\mathbf{dS}\}\tau - 2\alpha_3\alpha_4\{\mathbf{dS}^2\}\tau^2 \\ + 2\alpha_2\alpha_4\{\mathbf{dWS}\}\tau^2), \end{aligned} \quad (46)$$

$$\mathcal{E}_\mu^* = \left[ 1 - \frac{4}{3}\alpha_4^2(S\tau)^2(\alpha_3^2 - 3\alpha_2^2\mathcal{R}^2) \right]^{-1},$$

$$\mathcal{R}^2 = -\frac{\{\bar{\mathbf{W}}^2\}}{\{\mathbf{S}^2\}} = \left( 1 - 2\bar{c}_\omega \frac{\Omega}{S} \right)^2. \quad (47)$$

Thus, in the composite model the production-to-dissipation rate ratio is a function of  $\Omega/S$  and  $S\tau$ . By interchanging this dependency, the behavior of  $\Omega/S$  as a function of  $\mathcal{P}/\varepsilon$  and  $S\tau$ ,

$$\frac{\Omega}{S} = \frac{1}{2\bar{c}_\omega} \left[ 1 \pm \frac{1}{\alpha_2} \sqrt{\frac{\bar{\alpha}_1}{\alpha_4} \left( \frac{\mathcal{P}}{\varepsilon} \right)^{-1} + \frac{1}{3}\alpha_3^2 - \frac{1}{\alpha_4^2(S\tau)^2}} \right], \quad (48)$$

can be studied. Figure 8 shows the evolution of  $\Omega/S$  across the channel for the different rotation regimes and the three models considered. For the two rotating cases, several features are apparent. Starting from values near zero on the anticyclonic side (because  $S$  is high near the wall), the DNS results clearly show a plateau at  $\Omega/S=0.5$ , then quickly grow and change sign at the location of the maximum velocity ( $S=0$ ). On the cyclonic side,  $\Omega/S$  ( $<0$ ) then approaches zero with a  $y^{-1}$  behavior ( $S \sim -y$  in the relaminarized region). The figure shows that the CASMs closely follow the DNS results and accurately predict the location of maximum velocity. With (48), we can explain why the CASMs are able to predict such features, and we shall see that the reason is

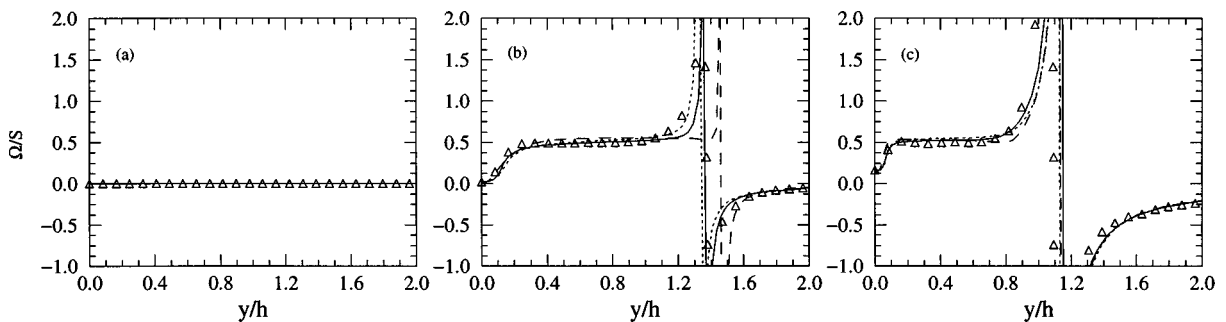


FIG. 8. Scaled rotation rate variation across channel for (a)  $Ro=0$ , (b)  $Ro=0.5$ , and (c)  $Ro=1.5$ .  $\Delta$  DNS (Ref. 4); —, CASM-SG; ---, CASM-HGJ; - - -, Coriolis-modified EVM.

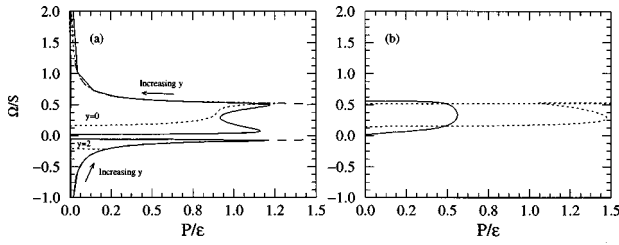


FIG. 9. Scaled rotation rate variation versus  $\mathcal{P}/\varepsilon$  in the channel for (a) CASM-SG and (b) Coriolis-modified EVM. —,  $Ro=0.5$ ; ---,  $Ro=1.5$ ; ···, limit branches (shown for (a) only).

closely related to the expression for  $\mathcal{E}_\mu^*$ , which shows the correct dependency on  $\Omega/S$  and  $S\tau$ , since by their nature, the CASMs, and more generally, all of the algebraic stress models that are consistently derived from Reynolds stress models inherit the correct behavior for  $\mathcal{E}_\mu^*$ .

For larger values of  $S\tau$  (i.e.,  $\geq 6$ ), the last term under the root in (48) is negligible compared with the other terms, and  $\Omega/S$  becomes a function of  $\mathcal{P}/\varepsilon$  only and takes values on the two limit branches that correspond to the sign of  $S$  ( $=\pm|S|$ ). Now, it is also easy to verify that these two values of  $\Omega/S$  rapidly become independent of an increasing  $\mathcal{P}/\varepsilon$ , and asymptote to either  $(\Omega/S)^+$  ( $S>0$ ) or  $(\Omega/S)^-$  ( $S<0$ ). Equation (48), therefore, shows that for a wide range of values of  $S\tau$  and  $\mathcal{P}/\varepsilon$  the value of  $\Omega/S$  becomes effectively independent of these parameters, and takes values close to  $(\Omega/S)^\pm$ . These two limiting values only depend on the values of the model coefficients  $\alpha_i$ 's, and for the SSG pressure-strain model are  $(\Omega/S)^+=0.496$  and  $(\Omega/S)^-=-0.057$ . In the channel away from the walls, the diffusion of  $K$  may be expected to be small, and we should have  $\mathcal{P}/\varepsilon \approx 1$  and  $S\tau \geq 6$ . In this case, the scaled rotation rate will have values on the limit branches that will be close to the limit values  $(\Omega/S)^\pm$ .

Figure 9 illustrates this phenomenon by showing the evolution of the scaled rotation rate correlated with the variation of  $\mathcal{P}/\varepsilon$  across the channel for the model CASM-SG and for the EVM. In Figure 9(a), the two limit branches given by (48) with values of  $S\tau \geq 6$  are represented by dashed lines. At  $\mathcal{P}/\varepsilon=0$  and  $y=0$ , the curves that correspond to the CASM calculations at the two rotation regimes first move in a region where  $(\Omega/S)^-<\Omega/S<(\Omega/S)^+$  because the values of  $S\tau$  that are given by the model are small. However, as  $\mathcal{P}/\varepsilon$  rapidly increases with movement away from the near-wall region,  $S\tau$  increases also, and the points collapse on the (positive) limit branch. Until very near the wall at  $y=2$ , the value of  $S\tau$  stays at values sufficiently high to force the points to stay on the limit branches. After having attained values close to  $(\Omega/S)^+=0.496$  for the major portion of the channel on the anticyclonic side, the maximum velocity point is reached,  $\mathcal{P}/\varepsilon$  becomes very small (as  $S \rightarrow 0$ ) and the negative limit branch is followed after the maximum velocity. For most of the values  $\Omega/S < (\Omega/S)^-$ , the corresponding value of  $\mathcal{P}/\varepsilon$  on the negative branch is very small, and according to (4), we can expect  $\partial K/\partial t < 0$ , which leads to relaminarization in this region.

This explanation for the occurrence of the linear profile

and the relaminarization process is also valid for other Reynolds stress models (i.e., other pressure-strain rate correlation models). For example, the Launder, Reece, and Rodi (LRR) model (Launder *et al.*<sup>18</sup>) yields limiting values for  $\Omega/S$  of  $(\Omega/S)^+=0.322$  and  $(\Omega/S)^-=-0.065$  for the anticyclonic and cyclonic sides, respectively, for the CASM-SG model. Therefore, one would expect that the slope of the linear velocity profile, when compared to DNS, would not be correct. Note also that these results are independent of the particular model for  $\varepsilon$  that is used, because the effect enters only through  $S\tau$  and  $\mathcal{P}/\varepsilon$ .

For the Coriolis-modified EVM,<sup>15</sup> relation (44) cannot be used to find a relation between  $\Omega/S$ ,  $\mathcal{P}/\varepsilon$ , and  $S\tau$ . Instead, the dissipation rate equation can be examined in regions away from the walls where the effect of the damping functions and of the diffusive terms can be neglected. The dissipation rate equation then yields the simple relation

$$\frac{\Omega}{S} = \frac{1}{4} \left[ 1 \pm \sqrt{1 - \frac{20}{(S\tau)^2} \left( \frac{C_{\varepsilon 1}}{C_{\varepsilon 2}} \frac{\mathcal{P}}{\varepsilon} - 1 \right)} \right], \quad (49)$$

where  $C_{\varepsilon 1}=1.44$  and  $C_{\varepsilon 2}=1.92$  for the Coriolis-modified EVM.<sup>15</sup> For sufficiently high values of  $S\tau$ , the dependency on  $\mathcal{P}/\varepsilon$  is totally removed, and  $\Omega/S$  takes a value of 0 or 0.5. Values of  $\Omega/S < 0$  can only be reached for vanishing  $\mathcal{P}/\varepsilon$  as shown in Figure 9(b). Thus, the model then yields an abrupt and total damping of the turbulence. (See Figure 5.)

The third test case to be studied is the pipe rotating axially at three different rotation rates.<sup>6</sup> In this case, rotation enters in a different way than in the previous cases studied. The rotating shear and rotating channel flow cases were studied in noninertial coordinate frames; while in the rotating pipe flow case the coordinate frame of reference is inertial and rotational effects enter through a boundary condition on a mean velocity component. This axisymmetric flow has a mean velocity field given by  $\bar{u}_i = (U(r), 0, U_\theta(r))$ , where  $U$  is the mean velocity component in the streamwise direction  $x$ , and  $U_\theta$  is the mean velocity component in the azimuthal direction  $\theta$ . In the fully developed regime considered here these velocity components are only a function of the radial coordinate  $r$ . This velocity field is more complex than the first two cases and leads to genuine three-dimensional mean strain rate and rotation rate tensors given by

$$S_{ij} = \frac{1}{2} \begin{bmatrix} 0 & \frac{dU}{dr} & 0 \\ \frac{dU}{dr} & 0 & \left( \frac{dU_\theta}{dr} - \frac{U_\theta}{r} \right) \\ 0 & \left( \frac{dU_\theta}{dr} - \frac{U_\theta}{r} \right) & 0 \end{bmatrix}, \quad (50)$$

$$\omega_{ij} = \frac{1}{2} \begin{bmatrix} 0 & \frac{dU}{dr} & 0 \\ -\frac{dU}{dr} & 0 & -\left( \frac{dU_\theta}{dr} + \frac{U_\theta}{r} \right) \\ 0 & \left( \frac{dU_\theta}{dr} + \frac{U_\theta}{r} \right) & 0 \end{bmatrix}.$$

The flow is parametrized by the bulk Reynolds number  $Re_b = RU_b/\nu$ , with  $U_b$  as the bulk velocity,  $R$  the pipe radius, and the rotation number  $N = U_{\theta,w}/U_b$  with  $U_{\theta,w}$  the azimuthal velocity at the pipe wall. The same numerical solution methodology used in the rotating channel flow case is also used for this flow with the appropriate modifications to account for the cylindrical coordinate system. Once again, 200 points were used in the radial direction, with highly stretched meshes near the pipe wall.

Because the different rotation regimes considered were obtained at the same bulk Reynolds number, the pressure gradient in the numerical code was adjusted in order to have  $Re_b = 10000$  at convergence. In the following, results for three different rotation numbers,  $N=0$ ,  $N=0.5$ , and  $N=1$  are shown. As before, the stress models studied are CASM-HGJ and CASM-SG, but the EVM used is the Launder-Sharma model<sup>17</sup> without the Coriolis modification. The Coriolis-modified EVM is excluded because it is perceived as an unfair test since the model was designed for the rotating channel flow case. In any case, the point about the insensitivity of linear EVMs to rotational effects has already been made. As with the channel flow case, all the models are integrated directly to the wall.

Figure 10 shows a comparison between the experimental and predicted streamwise and azimuthal mean velocity components across the pipe. The streamwise component is generally well-predicted by the CASMs while the EVM is only capable of predicting the non-rotating pipe flow. As expected the CASMs show the correct sensitivity to rotation. Further evidence of the composite model's ability to capture the correct rotation trends can be found in the expression for  $\mathcal{E}_\mu^*$  valid for this flow, and given by

$$\mathcal{E}_\mu^* = \left[ 1 - \frac{1}{3} \alpha_4^2 \left( \tau \frac{dU}{dr} \right)^2 (\alpha_3^2 - 3\alpha_2^2 \mathcal{R}^2) \right]^{-1}, \quad (51)$$

$$\mathcal{R}^2 = - \frac{\{\omega^2\}}{\{S^2\}} = \frac{1 + \left( \frac{dU_\theta}{dr} + \frac{U_\theta}{r} \right)^2 \left( \frac{dU}{dr} \right)^{-2}}{1 + \left( \frac{dU_\theta}{dr} - \frac{U_\theta}{r} \right)^2 \left( \frac{dU}{dr} \right)^{-2}}. \quad (52)$$

The expression shows that as the rotation rate of the pipe increases,  $\mathcal{E}_\mu^*$  decreases, causing a corresponding decrease in the turbulence. This is true across the pipe and is consistent with the experimentally observed trends.<sup>6</sup> These experiments have shown that the pipe rotation has a stabilizing effect on the turbulence, and as a consequence, an increase of the axial velocity was observed near the center, with a decrease near the wall. As the rotation number of the pipe increases, the shape of the axial velocity profile comes closer to the laminar one.

The azimuthal velocity profile is not a forced-vortex type, but has a concave shape. Unfortunately, neither CASM is able to capture the correct behavior of the azimuthal velocity component. This is consistent with recent computations<sup>19,20</sup> using ASMs which include cubic terms in the tensorial representation (18) for three-dimensional flows. These results showed that in order to deviate from the linear azimuthal profile found with the terms quadratic in the strain

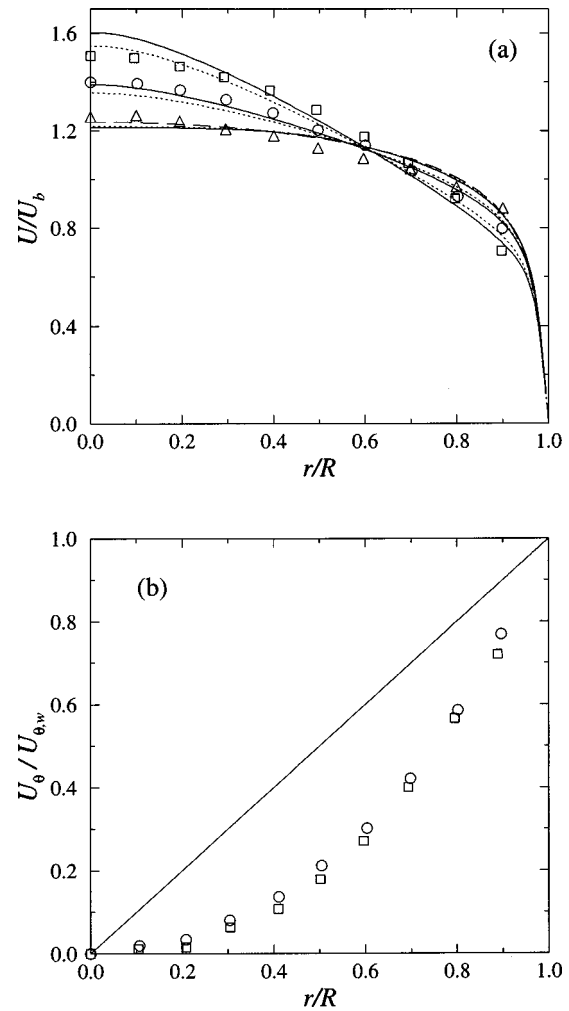


FIG. 10. Mean velocity variation across pipe: (a) streamwise component, and (b) azimuthal component.  $\triangle$ ,  $N=0$ ;  $\circ$ ,  $N=0.5$ ;  $\square$ ,  $N=1$ ; —, CASM-SG; ---, CASM-HGJ; ···, EVM.

and rotation rate tensors, higher order cubic terms in the strain and rotation rate tensors were needed. Since these other basis representations are not precluded by the present analysis, the methodology developed here can be extended to these alternative ASMs.

## V. CONCLUDING REMARKS

A composite algebraic stress model (CASM), which accounts for dissipation rate anisotropies, has been developed for application to flows in noninertial frames. It has been shown in the development of the composite model that different types of anisotropic dissipation models can be used, and two different models have been implemented and tested on rotating homogeneous shear flow, rapidly rotating, fully developed, channel flow, and axially rotating, fully developed, pipe flow. For the rotating channel flow case, a Coriolis-modified eddy viscosity model is also evaluated in order to contrast the performance of a phenomenologically based model with models more rigorously derived from stress and/or dissipation rate transport equations.

The performance of the CASMs has been analyzed and found to perform well in the rotating homogeneous shear

case, and the rotating channel and pipe flow cases. The model CASM-SG which is based on the Speziale and Gatski<sup>3</sup> anisotropic dissipation rate model performed better than the anisotropic model of Hallböck *et al.*<sup>9</sup> in the rotating homogeneous shear and channel flow cases. Both models outperformed the Coriolis-modified EVM even though it had performed successfully in previous studies at lower channel rotation numbers.<sup>15</sup> This shows that algebraic stress models consistently derived from Reynolds stress models can inherit the correct dependency to rotation, with noninertial effects automatically accounted for in a rigorous way. The study also demonstrated that the key features of the rotating channel flow were controlled by mechanisms only remotely linked to the isotropic dissipation rate equation, which would mean that phenomenological models that attempt to account for non-inertial effects solely through modification of the source terms in the isotropic dissipation rate equation may not be properly accounting for essential flow physics.

For the axially rotating pipe flow, both composite algebraic stress models captured the behavior of the streamwise velocity component at the different rotation rates, but yielded an incorrect linear profile for the azimuthal velocity component. Recent results have shown that tensorial representations for three-dimensional flows that are cubic in the strain and rotation rate tensors may be needed to correctly account for this azimuthal mean velocity variation. Such alternative basis representations can also be sensitized to additional anisotropic effects using the methodology presented here.

## ACKNOWLEDGMENTS

The authors thank Professor M. Deville for his encouragement and helpful discussions throughout this study. Both (T.J.) and (G.M.) greatly acknowledge the financial support from the Commission Suisse pour l'Encouragement de la Recherche Scientifique, and (T.J.) also acknowledges the support of Sulzer Brothers S.A. under Contract No. 3062.1. T.B.G. acknowledges the support of the ERCOFTAC Leonhard Euler Research Center while in residence at École Polytechnique Fédérale de Lausanne as an ERCOFTAC scientific visitor.

<sup>1</sup>T. B. Gatski and C. G. Speziale, "On explicit algebraic stress models for complex turbulent flows," *J. Fluid Mech.* **254**, 59 (1993).

<sup>2</sup>X.-H. Xu and C. G. Speziale, "Explicit algebraic stress model of turbulence with anisotropic dissipation," *AIAA J.* **34**, 2186 (1996).

<sup>3</sup>C. G. Speziale and T. B. Gatski, "Analysis and modeling of anisotropies in the dissipation rate of turbulence," *J. Fluid Mech.* **344**, 155 (1997).

<sup>4</sup>E. Lamballais, M. Lesieur, and O. Métais, "Effects of spanwise rotation on the stretching in transitional and turbulent channel flow," *Int. J. Heat Fluid Flow* **17**, 324 (1996).

<sup>5</sup>R. Kristoffersen and H. I. Andersson, "Direct simulations of low-Reynolds-number turbulent flow in a rotating channel," *J. Fluid Mech.* **256**, 163 (1993).

<sup>6</sup>S. Imao, M. Itoh, and T. Harada, "Turbulent characteristics of the flow in an axially rotating pipe," *Int. J. Heat Fluid Flow* **17**, 444 (1996).

<sup>7</sup>C. G. Speziale, S. Sarkar, and T. B. Gatski, "Modelling the pressure-strain correlation of turbulence: An invariant dynamical systems approach," *J. Fluid Mech.* **227**, 245 (1991).

<sup>8</sup>T. Jongen and T. B. Gatski, "General explicit algebraic stress relations and best approximation for three-dimensional flows," *Int. J. Eng. Sci.* (to be published).

<sup>9</sup>M. Hallböck, J. Groth, and A. V. Johansson, "An algebraic model for nonisotropic turbulent dissipation rate in Reynolds stress closures," *Phys. Fluids A* **2**, 1859 (1990).

<sup>10</sup>K. Hanjalić and B. E. Launder, "Contribution towards a Reynolds-stress closure for low-Reynolds-number turbulence," *J. Fluid Mech.* **74**, 593 (1976).

<sup>11</sup>J. Bardina, J. H. Ferziger, and W. C. Reynolds, "Improved turbulence models based on large-eddy simulation of homogeneous, incompressible turbulent flows," Stanford University Technical Report No. TF-19, 1983.

<sup>12</sup>C. G. Speziale and X.-H. Xu, "Towards the development of second-order closure models for non-equilibrium turbulent flows," *Int. J. Heat Fluid Flow* **17**, 238 (1996).

<sup>13</sup>S. Tavoularis and S. Corrsin, "Experiments in nearly homogeneous turbulent flows turbulent shear flows with a uniform mean temperature gradient," *J. Fluid Mech.* **104**, 311 (1981).

<sup>14</sup>J. Laufer, "Investigation of turbulent flow in a two-dimensional channel," NACA Technical Report No. 1053, 1951.

<sup>15</sup>J. H. G. Howard, S. V. Patankar, and R. M. Bordyniuk, "Flow prediction in rotating ducts using Coriolis-modified turbulence models," *J. Fluids Eng.* **102**, 456 (1980).

<sup>16</sup>B. A. Pettersson, H. I. Andersson, and S. Øyvulstad, "Modelling system rotation with an anisotropic eddy-viscosity closure," *Proceedings of the Second ECCOMAS Conference on Numerical Methods in Engineering*, edited by J.-A. Désidéri *et al.* (Wiley Interscience, New York), p. 683 (1996).

<sup>17</sup>B. E. Launder and B. I. Sharma, "Application of the energy dissipation model of turbulence to the calculation of flow near a spinning disc," *Lett. Heat Mass Transfer* **1**, 131 (1974).

<sup>18</sup>B. E. Launder, G. J. Reece, and W. Rodi, "Progress in the development of a Reynolds-stress turbulence closure," *J. Fluid Mech.* **68**, 537 (1975).

<sup>19</sup>S. Wallin and A. V. Johansson, "A new explicit algebraic stress turbulence model for 3D flow," *Proceedings of the Eleventh Symposium on Turbulent Shear Flows*, Grenoble, France, 1997 (unpublished), Session 13, p. 13.

<sup>20</sup>T.-H. Shih, J. Zhu, W. W. Liu, K.-H. Chen, N.-S. Liu, and J. L. Lumley, "Modeling of turbulent swirling flows," *Proceedings of the Eleventh Symposium on Turbulent Shear Flows*, Grenoble, France, 1997 (unpublished), Session 31, p. 1.